Three-dimensional (3D) and two-dimensional (2D) lead iodide-based perovskite materials: A comparison of material stability and ammonia gas sensitivity

Norfatihah Mohd Adenam [a], Muhamad Yuzaini Azrai Mat Yunin [a], Wan M Khairul [b], Abdul Hafidz Yusoff [a], Hasyiya Karimah Adli [c, d, *]

[a] *Faculty of Bioengineering and Technology, Universiti Malaysia Kelantan, Jeli, Kelantan 17600, Malaysia*
[b] *Advanced Nano Materials (ANoMa) Research Group, Faculty of Science and Marine Environment, Universiti Malaysia Terengganu, Kuala Nerus, Terengganu 21030, Malaysia*
[c] *Department of Data Science, Universiti Malaysia Kelantan, City Campus, Pengkalan Chepa, Kota Bharu, Kelantan 16100, Malaysia*
[d] *Institute for Artificial Intelligence and Big Data, Universiti Malaysia Kelantan, City Campus, Pengkalan Chepa, Kota Bharu, Kelantan 16100, Malaysia*

ARTICLE INFO

ABSTRACT

Despite enormous attention on lead halide perovskite, the stability of material is of major concern that is in critical needs of attention. Lead iodide-based $CH_3NH_3PbI_3$ (3D) perovskite (MIP) and $(H_2C=C(CH_3)CO_2CH_2CH_2NH_3)_2PbI_2Cl_2$ (2D) perovskite (AMP) were synthesised and investigated for different days under various storage conditions. After few days, the original surface morphology of both samples changed and small scattered particles were found. RMS (roughness) of MIP decreased from 51.78 to 18.00 nm, while AMP showed otherwise (from 37.70 to 95.52 nm). The increase in roughness favours the diffusion of ammonia gas molecules into perovskite and consequently increases gas response properties. Based on roughness, FWHM, crystallite size, crystallinity and lattice strain parameters, it can be concluded that 2D AMP exhibited better sensing properties than 3D MIP although the finding shows superior stability of 3D over 2D due to the self-crystallization of 3D perovskite materials.

1. Introduction

Lead halide perovskite $CH_3NH_3PbX_3$ (X = Cl, Br, I) have brought such important impacts in the scientific world in the past decades due to its strong light harvesting, high charge-carrier mobility and long charge-carrier diffusion length [1–3]. However, long term stability of lead halide perovskite remains a major challenge for practical application due to its vulnerability towards environmental elements such as humidity that leads to severe degradation over time [4–6]. Typically, lead-halide perovskite structure is in conventional three-dimensional (3D) form as shown in Fig. 1a, with the ABX_3 (A:anion, B: metal cation and X:halide) formula. Lead halide perovskite presents a great potential to become the leader in next-generation photovoltaic technologies [7]. Yet, the instability of 3D perovskite towards moisture and oxygen exposure is the main challenge for commercialization [8–10].

Meanwhile, two-dimensional (2D) perovskite has recently been identified as a promising material in terms of better stability and less defect passivation since 2D layered perovskite film contains long-chain organic cations. In particular, 2D possesses long-chain hydrophobic organic cations that ensure better stability and performance [12]. 2D exhibits promising long-term stability by exchanging alkyl halides, simple compositional substitution and variation of precursor solution [13–15]. Previously, 2D lead halide perovskite solution was reported based on the formula of $R_2(CH_3NH_3)n-1MnX_{3n+1}$ (R: organic group, M: metal cation and X: halide) [1,8] (Fig. 1b). Due to the longer alkyl chain, 2D structure has greater dielectric characteristics as long alkyl groups composed of high partial charge and dipole moments [16,17].

2D halide perovskites have gained interest due to their superior stability in ambient conditions with structural diversity and tunable optoelectronic properties [18]. Low dielectric constant of organic spacer cations of 2D leads to the confinement of charge carriers in quantum wells, which effect on the anisotropic optical and electrical properties of material. 2D halide perovskite has been approached as new dimension of perovskite as it has tunable photoelectric properties and environment

---

* Corresponding author at: Department of Data Science, Universiti Malaysia Kelantan, Kampus Pengkalan Chepa, Kota Bharu, Kelantan 16100, Malaysia.
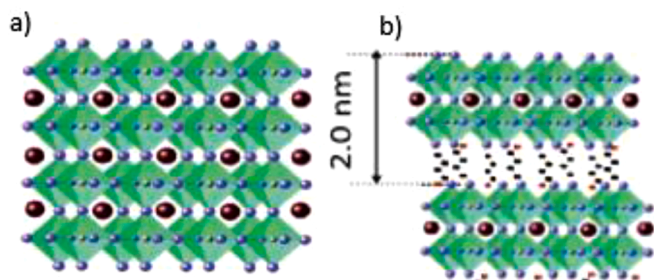*E-mail address:* hasyiya@umk.edu.my (H.K. Adli).

Fig. 1. Structures of: (a) three-dimensional (3D) lead halide perovskite and (b) two-dimensional (2D) lead halide perovskite [11].

stability compared to 3D perovskite [19,20]. It is formed by distortions from the cubic structure that can arise from the size-mismatch of the ions that contributed to the additional perovskite structures [21–23].

Recently, an inorganic halide and methylammonium lead perovskite material ($CH_3NH_3PbI_3$) with the structure of ABX_3 has drawn such attention from researchers because its ability to interact with gas in the atmosphere [24]. It has been addressed before that the changes of color of methylammonium lead perovskite after exposure to ammonia gas, which led to resistance change of materials [24,25]. The sensitive nature of photovoltaic in fact turns into opportunity for gas sensor application, which recently reported for detecting ammonia gas [26,27].

Previous studies have revealed the potential of perovskites as gas sensors for various types of gas analytes [26,28]. In terms of improving perovskite's stability, 2-aminoethyl methacrylate hydrochloride ($H_2C=C(CH_3)\ CO_2CH_2CH_2NH_2 \cdot HCl$) was used as ligand to stabilize perovskite by retaining the architecture of perovskite by allowing polymerizable groups (vinyl) on the surface of perovskites [29]. These perovskite-crosslinked networks reported as high air and water durability, as well as remarkable for high photoluminescence quantum yields [29,30].

Hence, in this study, an investigation was conducted to identify the difference in material stability between 2D and 3D lead-halide perovskites and evaluate their potential for gas sensor application. The objectives of the study are to synthesis a novel 2D-perovskite material (AMP) based on 2-aminoethyl methacrylate hydrochloride and to compare the 2D and 3D typical $CH_3NH_3PbI_3$ (methylammonium iodide perovskite) in terms of material stability over time under room temperature, silica and vacuum storage conditions. Few analysis such as optical microscope, X-ray diffraction and Atomic Force Microscope were conducted at day 1 (D1), day 15 (D15) and day 20 (D20). Then, application of AMP and MIP as ammonia gas sensors was also investigated based on XRD and AFM analyses by observing the changes in crystallinity, surface morphology and roughness parameters [31,32].

2. Experimental

2.1. Materials

Lead (II) iodide (Sigma Aldrich (M) Sdn. Bhd., Selangor, Malaysia) (99%) (PbI_2), methylammonium iodide (Sigma Aldrich (M) Sdn. Bhd., Malaysia) ($\geq$99.0%) (MAI), 2-aminoethyl methacrylate hydrochloride (Acros Organics) (90%, stabilized), titanium (IV) dioxide powder (R&M Chemicals) ($\geq$ 99.5%, 1 to 150 nm) and titanium diisopropoxide bis (acetylacetonate) (Sigma Aldrich (M) Sdn. Bhd., Malaysia) (75 wt. % in isopropanol) were used without further purification. Few solvents used for the reaction include *N,N*-dimethylformamide (Sigma Aldrich (M) Sdn. Bhd., Malaysia) (anhydrous, 99.8%), dimethyl sulfoxide (Sigma Aldrich (M) Sdn. Bhd., Malaysia) (anhydrous, $\geq$ 99.9%), ethylene glycol (5M, R&M Chemicals, Malaysia) and 2-propanol (Sigma Aldrich (M) Sdn. Bhd., Malaysia) (anhydrous, $\geq$ 99.5%). Indium Tin Oxide (Sigma Aldrich (M) Sdn. Bhd., Malaysia) (surface resistivity: 70-100 Ω/sq.) was

used as base for gas sensor devices.

2.2. Fabrication

Upon the preparation of the perovskite materials thin film, Indium Tin Oxide (ITO) conductive plate was undergone specific treatment as reported previously [12]. In this study, there are two types of titanium (IV) dioxide (TiO_2) were prepared as substrate layers of perovskite. Titanium (IV) dioxide (TiO_2) paste ($pTiO_2$) made from the solution of TiO_2 in ethylene glycol that undergone overnight stirring before forming off-white paste. After obtaining homogeneous paste, the dilution solution was prepared by mixing 1 mL of TiO_2 paste into 100 mL of ethanol.

A dense TiO_2 layer ($dTiO_2$) was deposited on the ITO/glass substrate in similar method reported elsewhere [9,10]. The $pTiO_2$ layer on $dTiO_2$-covered ITO/glass ($dTiO_2$/ITO/glass) was made by spin-coating a 50 μL solution of $pTiO_2$ at 2000 rpm for 20 seconds, followed by heating at 125°C and 550°C for 35 minutes. The resulted $pTiO_2/dTiO_2$/ITO/-glass was preheated at 500°C upon use.

For the synthesis of 3D methylammonium iodide perovskite (MIP), 1.2 M of PbI_2 was prepared in solvent mixture of N, N-dimethylformamide (DMF) and dimethyl sulfoxide (DMSO). Meanwhile, 0.025 M of methylammonium iodide (MAI) was prepared in 3 ml of 2-propanol solvent. Then, the solution of PbI_2 (90 μL) was dropped on preheated TiO_2/ITO glass, spin-coated at 4000 rpm for 30 seconds before immersed in solution of MAI for 30 minutes. Next, it was spin-coated at 2500 rpm for 30 seconds and finally annealed at 100°C for 20 minutes.

For the synthesis of 2D aminoethyl methacrylate perovskite (AMP), 0.42 M of PbI_2 was mixed with 0.83 M of AEMA before heated up until 100°C. TiO_2/ITO glass was immersed in this mixed solution for 30 minutes before spin-coated at 1000 rpm for 10 seconds, and continuously at 5000 rpm for 30 seconds and heated up until 200°C for 30 minutes. The process was re-run by immersing the film in mixed solution for 15 minutes and spin-coated again. The perovskite sample was then heated at 100°C for 10 minutes followed by 200°C for 1 hour.

The final substrates of MIP and AMP are shown in Fig. 2 which were prepared based on the fabrication method (Fig. 3). The samples were kept in different conditions which are at room temperature (25°C) (RT), silica (S) and vacuum (V). The samples were denoted as D1, D15 and D20 for day 1 (24 hours preparation), day 15 and day 20.

2.3. Characterization

To evaluate the changes of materials at D1 (after 24 hours preparation), D15 and D20 under different conditions, several physical characterizations were conducted using an optical microscope (OM), X-Ray Diffraction (XRD), atomic force microscope (AFM) and scanning electron microscope (SEM) analysis. Microstructure morphologies of MIP and AMP were checked using ProgRes Microscope Cameras (Jenoptik, Jena, Germany) at 50 × magnification. The crystallite size, crystalline structure and lattice strain were evaluated from X-ray diffraction spectra (XRD D2 Phaser) (Bruker, Shah Alam, Malaysia) under monochromated Cu Kα irradiation (λ = 1.5418 Å) at 4°C min^{-1} from 10° until 90°. AFM analysis was carried out using Zetasizer (Nanoseries Model ZEN 3600 AFM) (Malvern Instruments, UK) via dynamic light scattering method to identify the changes of surface morphologies of samples at Day 5 before and after ammonia gas exposure. For surface morphology of perovskites, SEM analysis using SEM-EDX (Quanta 450) (Field Electron and Ion Company, FEI, Oregon) at 200 μm magnification was done before and after ammonia gas exposure that conducted at room temperature in various durations from 1 min, 3 min, 5 min and 10 min.

For gas sensor application, MIP and AMP (D1 samples) underwent a direct exposure for 5 min at a constant flow of 99.99% ammonia gas (Sani Sdn. Bhd.) (NH_3) in a sealed vessel. Fig. 4 shows the general illustration for the process of NH_3 gas exposure on the samples. Both samples were inserted individually into the test chamber before purified nitrogen gas (99.99%, Dira Resources) was purged at 10 sccm (standard
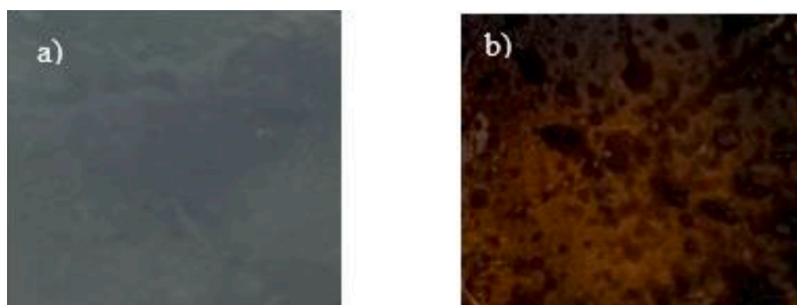
Fig. 2. Samples of: (a) MIP and (b) AMP.

a) Synthesis of **MIP**

| Spin-coated at 4000 rpm, 30 seconds after dropping 90 µL **PbI₂** on TiO₂/ITO glass | Immersed sample in **MAI** solution for 30 minutes | Spin-coated at 2500 rpm, 30 seconds | Annealed for 20 minutes at 100 °C |

b) Synthesis of **AMP**

| Immersed TiO₂/ITO glass in mixed solution of **AEMA** for 30 minutes | Spin-coated at 1000 rpm, 10 seconds followed by 5000 rpm, 30 seconds | Annealed at 100 °C for 10 minutes followed by 200 °C for 1 hour |

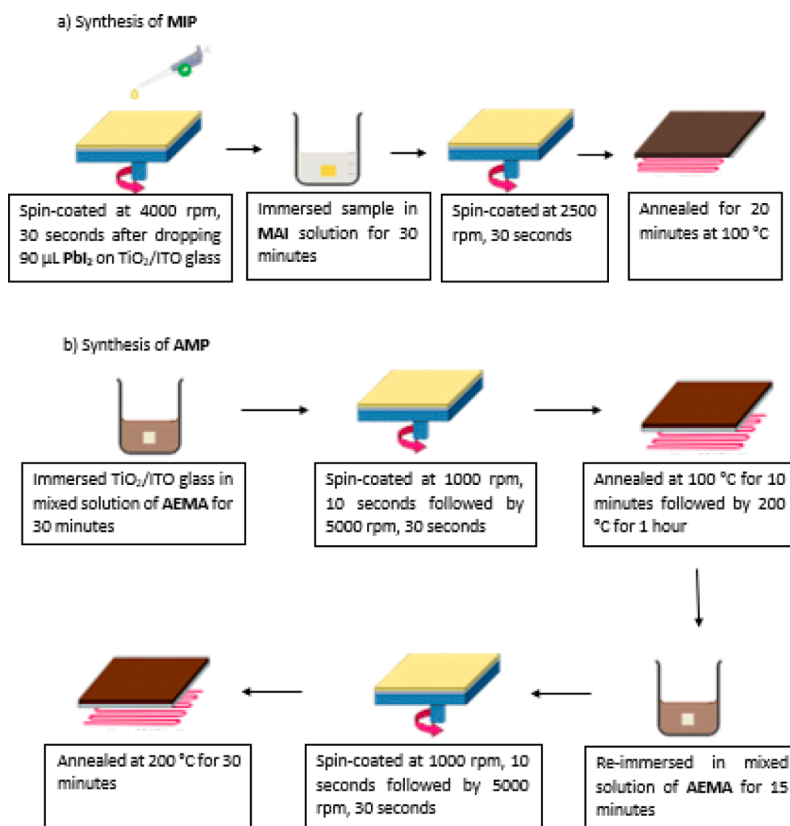| Annealed at 200 °C for 30 minutes | Spin-coated at 1000 rpm, 10 seconds followed by 5000 rpm, 30 seconds | Re-immersed in mixed solution of **AEMA** for 15 minutes |

Fig. 3. Fabrication process for: (a) MIP and (b) AMP.

cubic centimetres per minute) for 15 minutes. NH_3 gas was then flow-in into the chamber to expose the sample to the gas for 5 minutes. After the exposure, N_2 gas was re-purged for 10 minutes to flush NH_3 gas into the vessel containing acid sulphuric neutralization (Fig. 4). The difference in crystallite size, crystallinity and lattice strain before and after gas exposure were identified and calculated from XRD spectra while roughness and surface morphology parameters were observed using AFM images and SEM images respectively.

3. Results and discussion

3.1. Optical microscope

Surface morphology of particle size and shape was observed using an optical microscope (OM) for all samples that kept under room temperature (RT), silica (S) and vacuum (V) at various days (D1, D15 and D20), respectively (Fig. 5).

Both samples exhibited distinct characteristics for different days of storage and under different conditions. For MIP, under all conditions,

samples showed needle-like shape except for sample under V that appeared as small particles. Similar surface morphology was reported previously in which the needle-like particles represent PbI_2 materials [33,34]. However, it can be seen that the crystal needle-like particles were found to diminish over few days.

In terms of surface morphology, MIP morphology exhibited in different shape compared to AMP. AMP appeared as small particles scattered on the surface with irregular shape, as reported from SEM morphology [35,36]. It is reported that the presence of AEMA acts as ligands that linked to the size and shape of the perovskites layer [37]. Particles of sample kept in V were identified with irregular shape. Disordered morphological features under V could be explained to the decomposition of crystalline perovskite [38,39].

Every condition was affected by environmental elements including moisture, oxygen, light and heat (Seok et al., 2020). However, several studies reported moisture can retard the crystallization of perovskite films in which slow and complete inter-diffusion of precursor element would occur [19,40]. Excessive water or moisture may degrade the perovskite material, while light and oxygen can also accelerate the
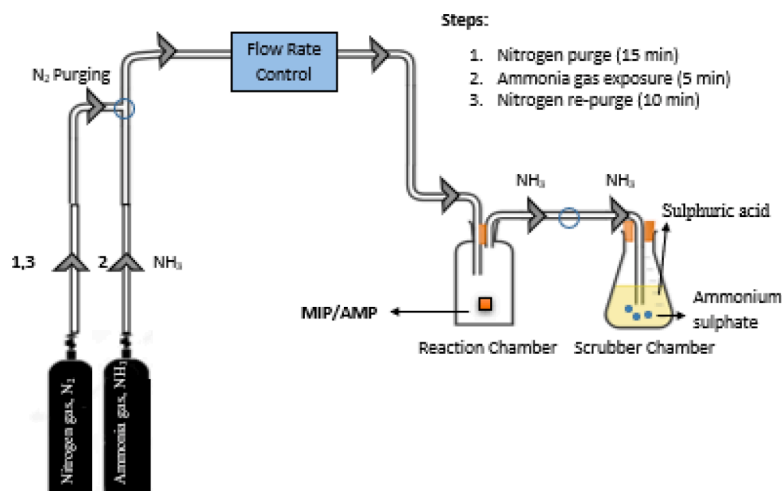
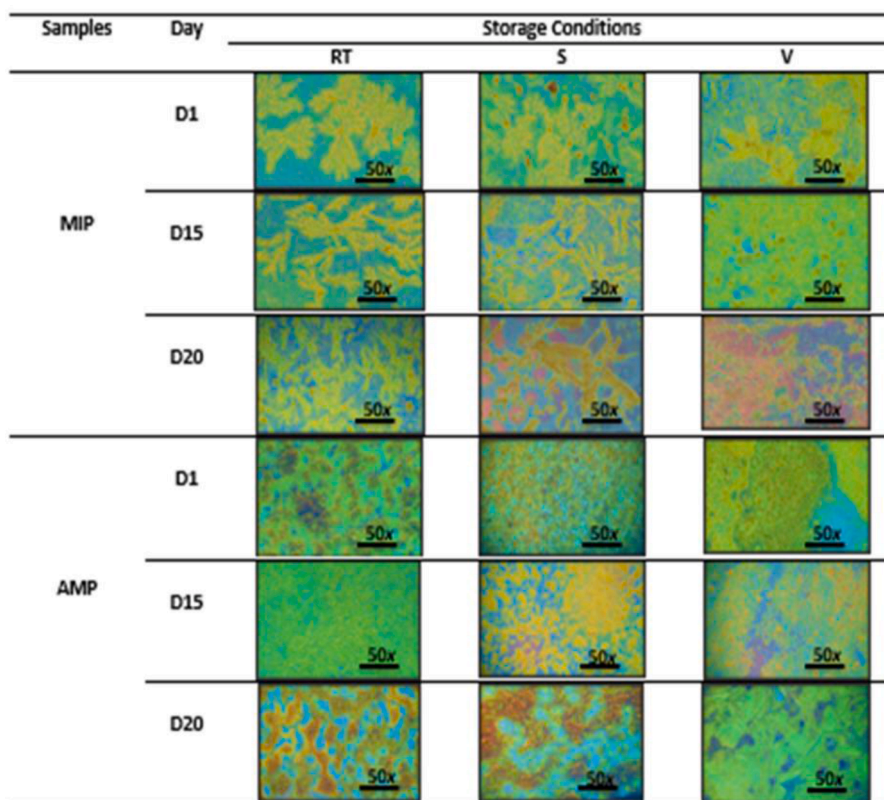**Fig. 4.** Process flow for the ammonia gas sensor application [12].

Fig. 5. Optical morphology of MIP and AMP at room temperature (RT), in silica (S) and in vacuum (V) for D1, D15 and D20.

process [41].

3.2. X-ray diffraction

3.2.1. Structural and crystallinity

X-ray diffraction was performed to check the structural properties of different dimension types of inorganic perovskite that used lead-iodide as the starting material namely AMP and MIP at different durations namely D1, D15, and D20. Results of the analysis revealed that the peak of the spectrum of final product exhibited a correlation with the lattice planes of the inorganic perovskite as shown by diffraction peak at 24.8° which corresponded to the (101) lattice planes of inorganic perovskite.

For MIP, all samples exhibited primer peaks of perovskite at 24.8° (101) and PbI_2 at 12.5° (001) and 38.9° (004) in similar peak locations as reported by other studies [42,43]. From (Fig. 6), it can be noted that there is only a little shift in MIP peak at 24.8° (101) for condition of S.

In Fig. 7, for AMP, it can be noticed that the gradual decrease in perovskite peaks (101) correlate with the increase in the PbI_2 peaks (001) (● marks peaks) after several days [44]. After 24 hours of preparation, the intensity of the PbI_2 peak was higher than the perovskite, suggested that the prompt transformation of the compound into a by-product was occurred [12]. The decline in perovskite peak (101) intensity and increase in PbI_2 peak (001) intensity became apparent at later days, with the intensity of perovskite peak (101) decreasing and
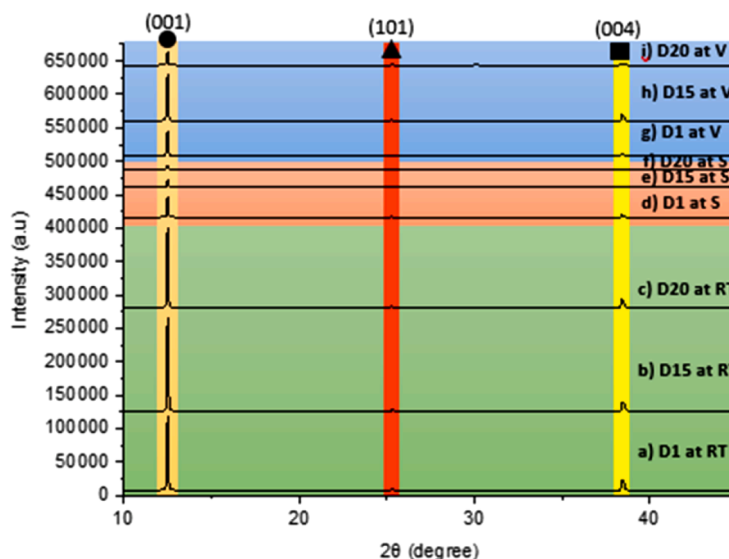
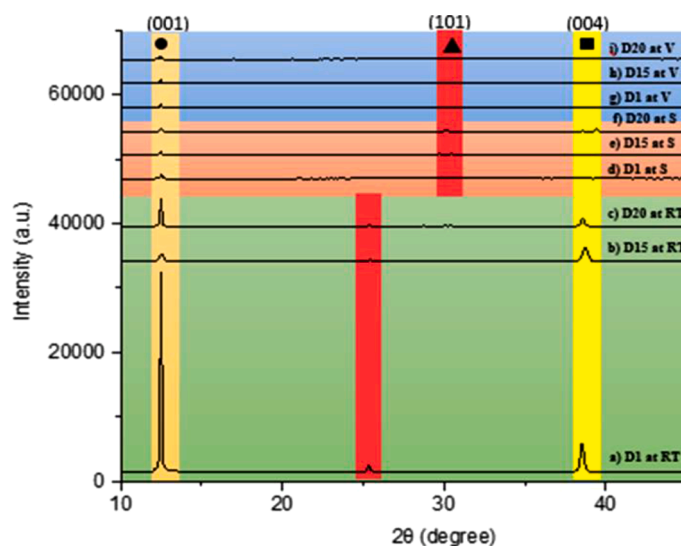**Fig. 6.** XRD spectrum of MIP shows ● for PbI_2 (001), ▲ for perovskite (101) and ■ for TiO_2 (004).

Fig. 7. XRD spectrum of AMP shows ● for PbI_2 (001), ▲for perovskite (101) and ■ for TiO_2 (004).

PbI_2 peak (001) increasing. There was a shift of peak location of AMP (101) and (004) at conditions of S and V although there was no noticeable change in PbI_2 peak (001) intensity over the duration for all conditions. The peak intensity of perovskite plane (101) decreased with the increase in time and the shift resulted mainly because of strain/stress present in the lattice [12,45]. These observations suggested that moisture-induced breakdown had altered the crystallographic structure of perovskites [46]. As perovskite crystal decomposition turn to PbI_2, it could be seen that PbI_2 peak (001) increase with the decline of the intensity of perovskite (101) peak (Fig. 7).

Hence, AMP shows high crystallinity under RT condition while under S and V conditions, the spectra were appeared as amorphous and broaden spectrum. However, the intensity for all peaks of MIP was higher than AMP. Whilst, stability of AMP and MIP deteriorated over time as most of organometallic perovskite from halide group would break down into hydroiodic acid (HI), methylamine (CH_3NH_2) and PbI_2 in the presence of water moisture (H_2O) or oxygen (O_2) [12].

Fig. 8. shows the plot of full width at half maximum (FWHM), crystallite size, crystallinity and lattice strain of MIP (●●●●●) and AMP (□) recorded at various durations in different conditions. FWHM is used

to calculate the crystallite size and lattice strain using Scherrer equation [47] based on XRD peaks as stated in Formulas (1) and (2) below:

$$D = \frac{k\lambda}{\beta cos\theta} \tag{1}$$

$$\varepsilon = \frac{\beta cos\theta}{4} \tag{2}$$

where D is average crystallite size (nm), k is Scherrer constant (0.89), λ is wavelength of the incident X-rays (0.154 nm for Cu Kα radiation), β is FWHM of the reflection peak which represents the diffraction pattern (in radians), θ is Bragg diffraction angle (in degrees) and ε is lattice strain (in percentage).

From Fig. 8a, it can be noticed that FWHM values of MIP decreased over time under all conditions except for S that increased from D1 to D15 but declined at D20 while AMP showed otherwise. Linear increase of FWHM can be explained because of the density of point defects that affect crystallinity, crystallite size and lattice strain [12]. This shows that FWHM varies inversely with crystallite size, with XRD peak becomes broader as crystallite size decreases. Thus, it may be deduced that as
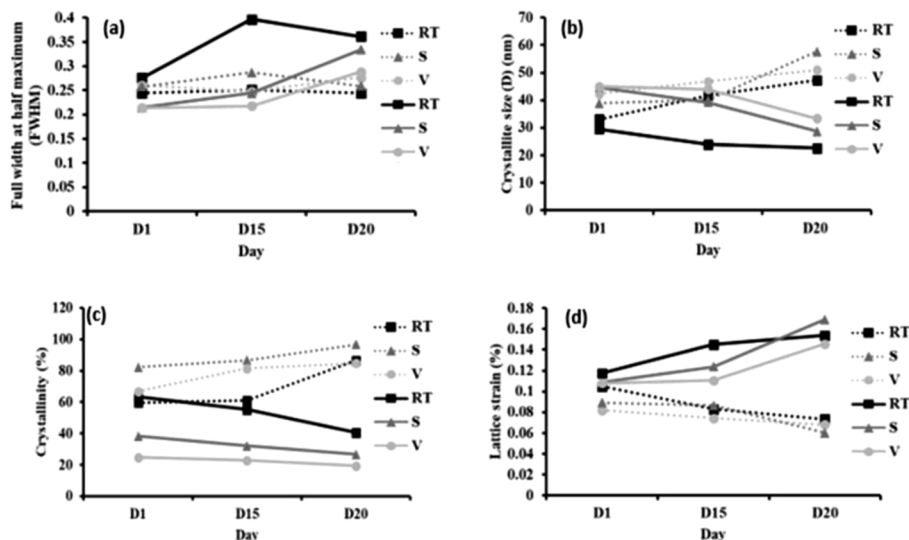
Fig. 8. Parameters of: (a) full width at half maximum (FWHM), (b) crystallite size, (c) crystallinity, and (d) lattice strain of MIP (●●●●●) and AMP (□) with ■ marked for RT, ▲ marked for S and ● marked for V.

FWHM values rise, the size of perovskite crystallites decreases.

As expected, increasing trends of MIP crystallite size was found as FWHM values decreased (Fig. 8b). MIP crystallite size under all conditions became bigger with course of time from 30 nm to 50 nm from D1 to D20 while AMP showed otherwise. The perovskite degradation leads to the phase segregation, morphological changes, and lattice shrinkage and crystallite size reduction [38]. Thus, AMP was found to be less stable compared to MIP. This reveals that peak width (FWHM) is inversely proportional with crystallite size, with the peak (101) (Fig. 7) becoming broader as crystallite size decreases, revealing the amorphous structure of the XRD spectrum. It may be deduced that as FWHM values rise, the size of perovskite crystallites decreases.

To evaluate the ratio of intensity from crystalline peaks to the sum of the crystalline and amorphous intensities, the crystallinity percentage is determined based on Formula (3):

$$I_o = \frac{I_{crystalline}}{I_{total}} \times 100 \tag{3}$$

where I_o is crystallinity in percentage (%), $I_{crystalline}$ is area of crystalline peaks and I_{total} is total area of peaks.

From the formula, MIP showed improved crystallinity from D1 until D20 under all conditions (Fig. 8c). At D1, the crystallinity of AMP exhibited highest value under RT condition at 63.57%, than only 38.35% and 24.84% for S and V [12]. However, the crystallinity of AMP was kept decreased from 63.57% to 40.50% for RT, 38.35% to 26.77% for S and 24.84% to 19.31% for V in the course of time until D20 [12]. It is reported that crystallinity is related to crystallite size, whereby smaller crystallite size exhibits less crystallinity [48]. Decrease in crystallinity over time was expected for all samples, suggesting the occurrence of perovskite degradation [12,48].

Lattice strain (Fig. 8d) of AMP increased for all conditions from D1 until D20 influenced by the decrease in crystallite size [12]. MIP lattice strain was decreased gradually after several days when crystallite size increased. The lattice strain indicated that atoms of the material were removed from their original lattice position [12,49]. Overall, MIP is more stable than AMP due to its crystal structure having continuous 3D perovskite network structure while 2D perovskite in the structure of edge-sharing of octahedral layers and cations packed in the voids between the layers [50]. The continuous network structure in 3D perovskite compared to 2D perovskite that has long alkyl chain makes 3D perovskite a better candidate due to its superior stability. The arrangement of long-chain has a weak force between neighbouring inorganic

layers and large distance between the layers may be adverse effect on the stability of the 2D [16,20]. Besides, researchers also highlighted that there is self-crystallization phenomenon in 3D perovskite that makes the diffraction peaks become stronger and improves material stability [51].

3.2.2. Effect of ammonia gas exposure

3.2.2.1. Structural and crystallinity. AMP and MIP films were exposed to ammonia gas (NH_3) to observe any structural changes using X-Ray Diffraction (XRD) analysis. Fig. 9 and Fig. 10 show the comparison of XRD spectra of MIP and AMP before (A) and after (B) gas exposure.

For the case of MIP (Fig. 9), it shows that the diffraction peak of PbI_2 (001) at 12.5° shifted and few peaks appeared at diffraction peaks of perovskite (101) at 25.35° after ammonia gas exposure [12]. These results were due to a cation exchange in the presence of an NH_3 gas molecule, as well as an electron transfer from an ammonia molecule to a nitrogen-bound hydrogen atom during the transition of MIP to NH_4PbI_3. After the exposure, the XRD peak of PbI_2 at 12.5° was indistinguishable from the background signal [52] as it shifted due to the decrease in perovskite peak intensity (101) (Fig. 9). It can be seen that the surface morphology of MIP changed from grey to yellow. Hence, it can be said that exposure to ammonia gas caused a permanent change in the MIP crystal structure [12].

Meanwhile, AMP (Fig. 10) also showed similar trend as MIP. A broaden peak was observed around 24.2° (Fig. 10B) that was identified as NH_4PbI_3 based on published data [53]. This indicated a complete breakdown and material change of AMP was occurred [12]. The surface morphology and roughness parameters of AMP also show the potential of AMP as gas sensor in which surface-to-volume ratio provides more adsorption sites on the surface for adsorbed gas and thus increase the interactions with gas molecule and sensitivity [54].

Both samples were further investigated based on full width at half maximum (FWHM), crystallite size, crystallinity and lattice strain (Fig. 11) to observe the changes of perovskite material upon ammonia gas exposure.

From Fig. 11a, an FWHM value of MIP was found decreased after exposure while AMP shows otherwise. As FWHM for MIP decreased (Fig. 11b), crystallite size of perovskite increased from 33.36 nm to 40.73 nm, while for AMP, crystallite size of perovskite decreased (Fig. 11b) from 29.49 nm to 1.61 nm. The reduction of crystallite size can be explained due to perovskite deterioration because of phase segregation, morphological deformation and lattice shrinkage [12]. In
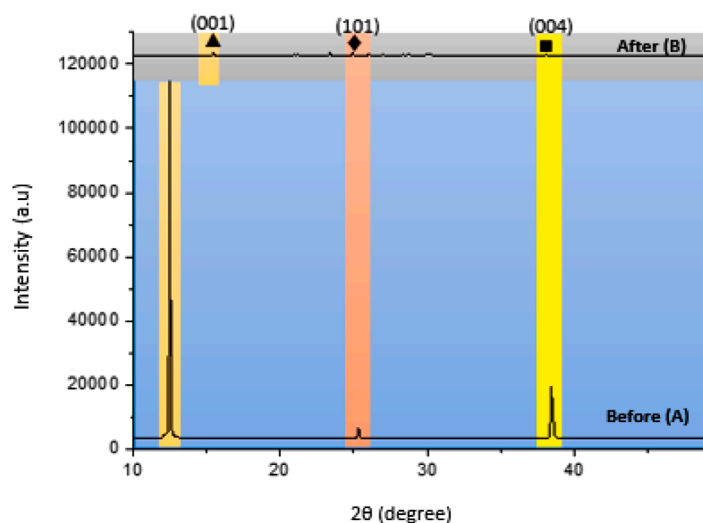
Fig. 9. XRD spectrum of MIP with ▲, ◆, ■ represent PbI_2 (001), perovskite (101) and TiO_2 (004).
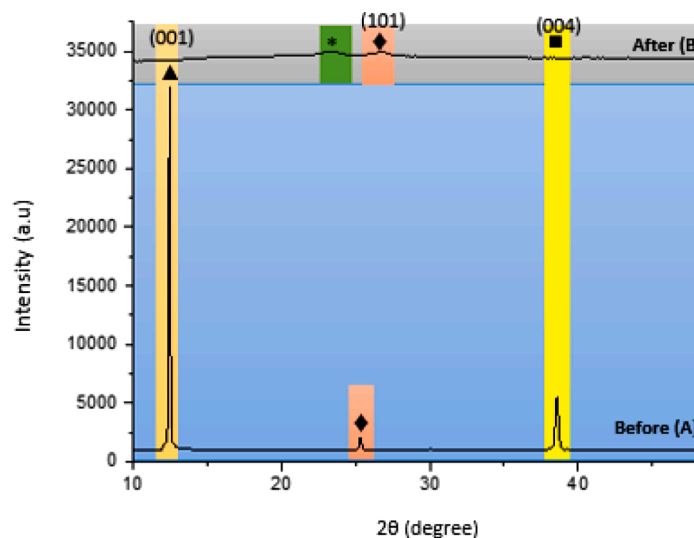

Fig. 10. XRD spectrum of AMP with ▲, ◆, ■ and * for PbI_2 (001), perovskite (101), TiO_2 (004) and new phase peak.

contrast to MIP, the crystallite size was increased, affecting the grain size and crystallinity since it is made up of agglomerations of crystallite [12]. As shown in Fig. 11c, crystallinity of MIP increased from 38.35% to 43.71% while crystallinity of AMP dropped from 63.57% to 30.78% after exposure. Other researchers also reported that structural lattice parameters decrease with increase in crystallite size [55]. Hence, the increase in AMP lattice strain (Fig. 11d) after exposure is related to the reduced in crystallite size. Incomparable pattern was noticed for MIP, whereby the lattice strain was found to reduce [12].

From the findings, it can be stated that AMP has better potential in comparison to MIP due to the advantage of 2D perovskite structure from staggered arrangement and organic cations tails between adjacent inorganic layers which connected by a weak force of van der Waals forces [12]. In addition, MIP has methylammonium ($CH_3NH_3^+$) cations that easily undergo decomposition when exposed to humid air forming ($CH_3NH_3PbI_3.H_2O$) and ($CH_3NH_3)_4PbI_6.2H_2O$. Meanwhile, AMP from ($2H_2=C(CH_3)CO_2CH_2CH_2NH_3^+$) cations have hydrophobic properties arising from the aliphatic or aromatic based organic spacers caused better material stability [56]. This arrangement also beneficial towards the sensitivity of 2D perovskite towards ammonia gas [16,53].

3.2.2.2. Surface roughness. Atomic Force Microscopy (AFM) was used as complement to study point-by-point topographic images [57] in order to observe the morphological features of MIP and AMP at D5 after 5 minutes of ammonia gas (NH_3) exposure.

As shown in Fig. 12, the prepared perovskite materials composed of grains size in the range of 200 until 920 nm. Grains size of MIP is larger than AMP (MIP: 335 nm, AMP: 240 nm) (Fig. 12 (a) and (b)) [15,58]. This may be due to the cubic-symmetry structure of MIP that has octahedra linked to each other via the vertex sharing, while AMP materials possess a lateral structure with the side length of up to microscales [15]. The result is in accordance to OM analysis which MIP exhibits bigger particles in the shape of needles and particles, compared to small particles that dispersed on TiO_2 for the case of AMP. Degradation that occurred caused MIP to become rougher compared to AMP. This can be explained by the fact that MIP is less stable and more vulnerable towards environment elements such as humidity [4,6].

As expected, after ammonia gas exposure, the morphology of both samples changed and the grains size turned bigger, which for MIP increased from 334.90 to 911.73 nm and AMP increased from 239.23 to 550.40 nm (Fig. 12 (e) and (f)). Based on previous report, this is because of the decomposition of perovskite materials upon specific gas exposure [59]. It was reported that the exposure to ammonia gas caused chemical reaction between methyl ammonium (MA) ions of perovskites with
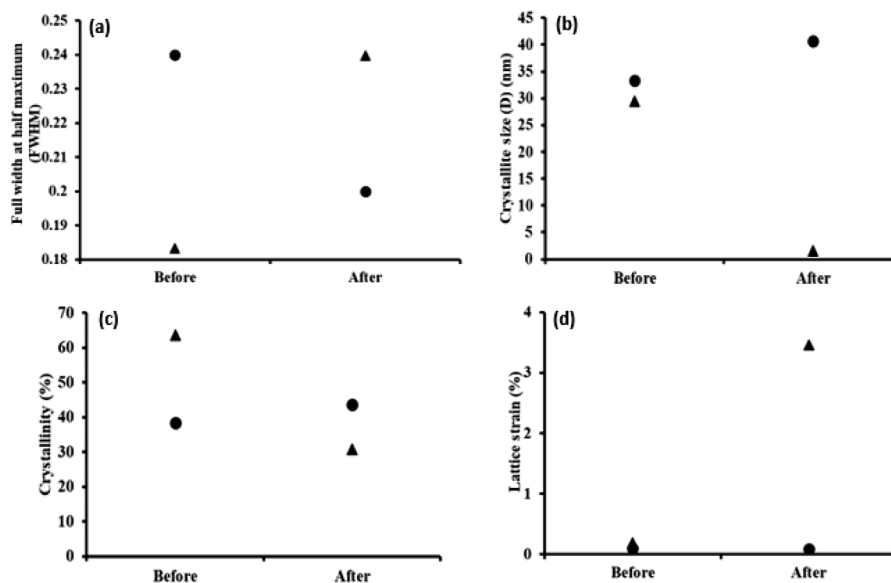
Fig. 11. (a) FWHM, (b) crystallite size, (c) crystallinity and (d) lattice strain of for MIP (●) and AMP (▲), before and after exposure.
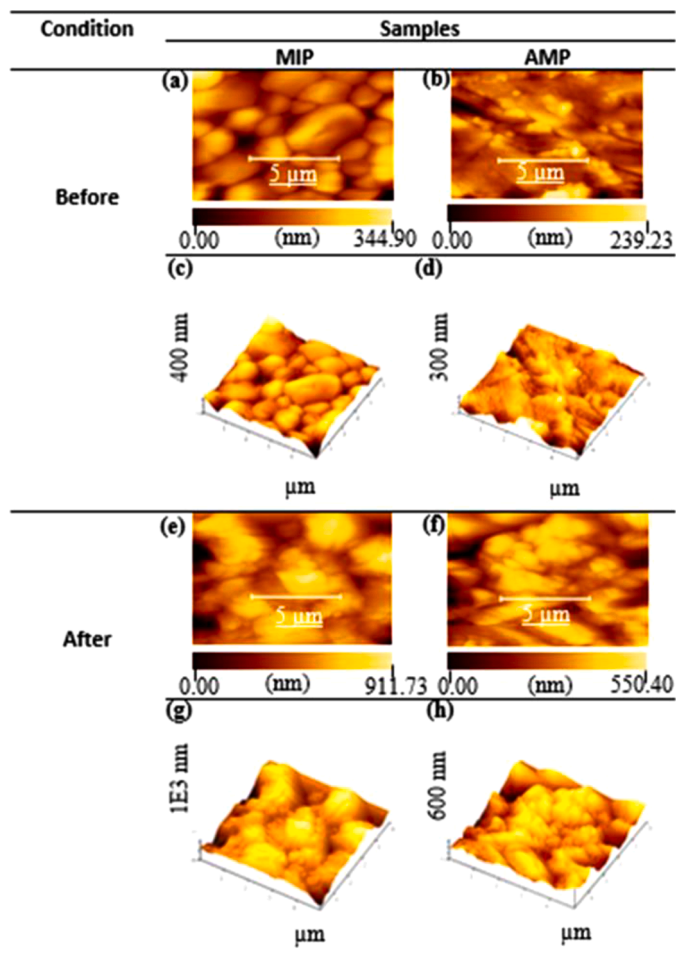

Fig. 12. Changes of morphology (a, b, g, h) and RMS (c, d, g, h) of MIP and AMP before and after gas exposure.

size of perovskite [24,59].

Meanwhile, roughness of surface material was also calculated (Fig. 12 (c), (d), (g) and (h)). It is measured by root mean square (RMS) defined as the increase in area due to interaction between the active semiconductor material of perovskite and ammonia gas [28]. In this case, two parameters were evaluated which are average roughness (R_a) and ten-point mean height (R_z). R_a is the mean height calculated over the entire measured length/area of the perovskites while R_z is based on the difference in height between the average of five highest peaks and five lowest valleys in the evaluation profile/surface [60,61]. The roughness parameters of both samples are summarized in Table 1.

Based on Table 1, values of MIP decreased from 51.78 to 18.00 nm, while AMP increased from 37.70 to 95.52 nm. RMS roughness of MIP decreased after exposure while AMP shows otherwise. Values of R_a and R_z, exhibit the same trend of RMS which represent good description of the overall roughness of surface as high values show higher roughness [62,63]. The increase in surface roughness increases the surface-to-volume ratio that facilitates more adsorption sites on the surface for adsorbed gas species and thus increase rate of interactions with gas molecule and sensitivity [54]. The roughness of AMP increased compared to MIP highlighting its greater potential as ammonia gas sensor. The roughness of MIP decreased may be due to its self-crystallization [51], as the perovskite deposited on the substrate is thermodynamically unstable and becomes easily converted to PbI_2 [15]. Besides, the roughness of MIP can also be explained by PbI_2 formation after severe degradation due to gas exposure. It is well confirmed that surface morphology and roughness of gas sensor material represent the potential for gas sensing applications [28,64].

3.2.2.3. Surface morphology. Morphological changes of MIP and AMP were also observed to compare before and after ammonia gas exposure that conducted at room temperature in various durations from 1 min, 3

ammonia gas. A-site of MA perovskite is replaced with ammonia ions (NH_4^+) that could dissociate MA molecules with PbI_2. Weak bonding between MA and PbI_2 causes the bond to broke and thus affect the grains

Table 1
Roughness parameters for MIP and AMP.

Gas exposure	Sample	RMS (nm) ($5 \times 5 \ \mu m^2$ sample)	R_a (nm)	R_z (nm)
Before	MIP	51.78	39.11	22.84
	AMP	37.70	27.52	23.56
After	MIP	18.00	14.17	55.10
	AMP	95.52	75.58	37.71

*Remarks: RMS represents the root mean square roughness, R_a is average roughness and R_z is ten-point mean height.

min, 5 min and 10 min (Fig. 13).

As shown in Fig. 13, slight change can be seen in the film surface for both samples after ammonia gas exposure. After exposure, the surface morphology of the film was found to be more random and rougher compared to homogeneous morphology before gas exposure. This type of morphological change is also reported elsewhere [24,65–67].

For the case of MIP, SEM images exhibited almost similar structural morphology as optical microscope images (Fig. 5). The sample that initially exhibited needle-like shape in the chain structure was turned to rough chained structure after several minutes of gas exposure. It can be explained that the film morphology properties strongly depend on the gas exposure time [68]. The SEM images represent that there is a slight agglomeration of perovskite grains after several minutes of gas exposure due to the reversible formation of NH_4PbI_3 and reconstruction of $CH_3NH_3PbI_3$ grains [69]. Gas exposure caused conversion reactions where by the gas can oxidize the I^- ions in the inorganic sheets to I_2, while generating NH^{4+} ions that coordinate to the Pb^{2+} centers [24,70].

The small particles scattered on the surface with irregular shape in the chained structure on the substrate turned into a fibrous shape after gas exposure [35,36]. There is significant variation in the porosity of the perovskite surface was observed. The porosity can facilitate the diffusion process and enhances the interaction between ammonia gas molecules and the perovskite surface [71]. The porous morphology provides a high surface area, which is important for improved sensitivity of ammonia molecules [24,69]. This SEM morphology trend has found related to the finding from AFM previously. Based on Table 1, average roughness (Ra) of MIP decreased significantly after gas exposure while AMP showed otherwise. The roughness of samples is another factor that has strong influence on the sensing capability of a sensor [72,26]. A rougher surface and larger surface to volume ratio of AMP allows more gas molecules to contact and react with the sensing film [26] to finally yield better sensing response.

4. Conclusion

A novel lead-iodide based perovskite of two-dimensional (2D) aminoethyl methacrylate was successfully synthesised to be compared with typical three-dimensional (3D) methylammonium for ammonia gas
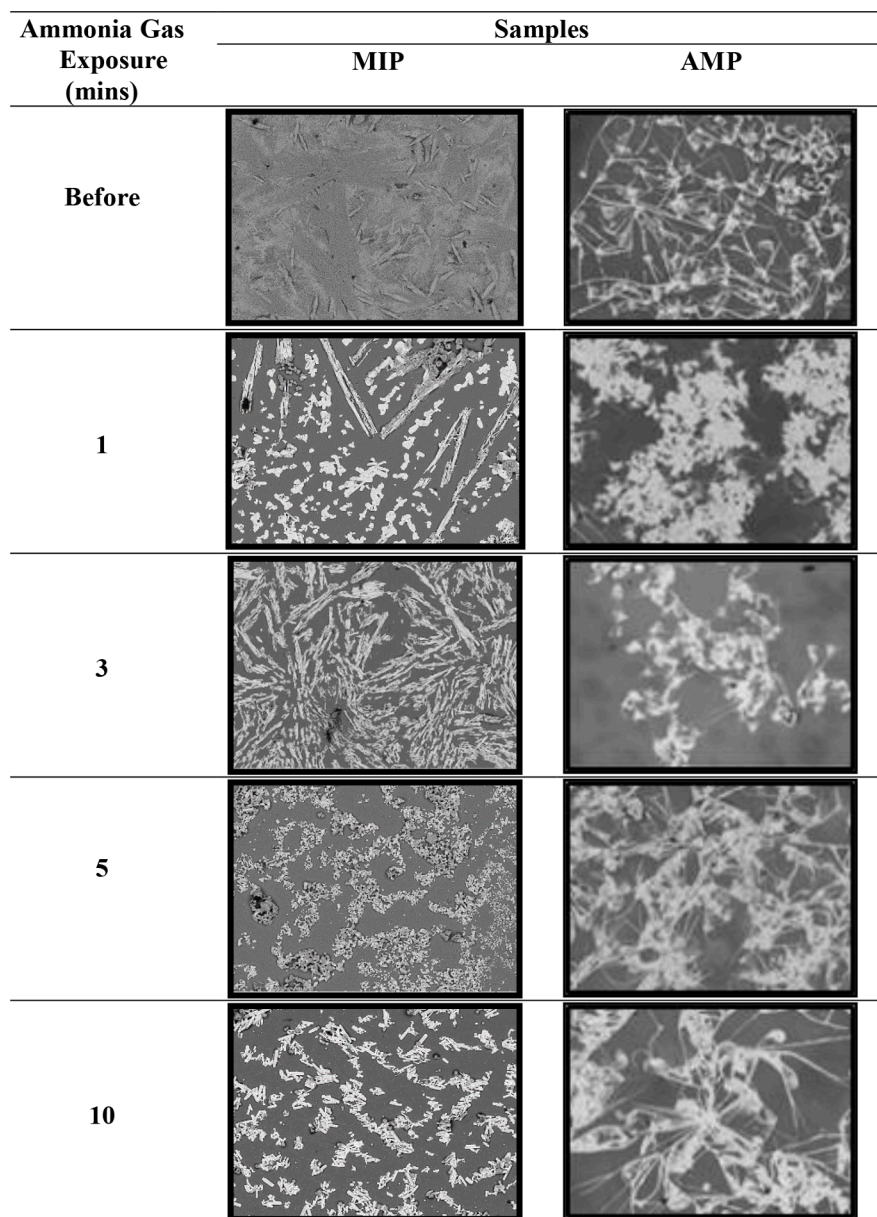

Ammonia Gas Exposure (mins)	Samples	
	MIP	AMP
Before		
1		
3		
5		
10		

Fig. 13. Surface morphology changes of MIP and AMP in different durations of exposure (1, 3, 5 and 10 mins).

sensing applications. The difference in physical properties and their stability were identified for few days from Day 1 until Day 20 in different storage conditions. From OM, the images show the changes of surface morphology of samples after few days. For MIP, needle-like shape could be seen while for AMP, irregular and scattered small particles were recorded. XRD spectrum proved that the formation of perovskite in both samples with the peak existence (101) at around 25.35°. The increase in crystallite size and crystallinity with time confirmed the increase in the stability of MIP materials, whilst, for AMP, the result shows otherwise. In order to observe the structural changes of MIP and AMP and their potential application as ammonia gas sensors, XRD analysis and AFM analysis were conducted. Formation of NH_4PbI_3 from the MIP spectrum, same goes to AMP indicating that complete breakdown of MIP and AMP have occurred. For the case of MIP, the diffraction peak of PbI_2 (001) at 12.5° was shifted and few peaks appeared in the region of diffraction peaks of perovskite (101) at 25.35° after ammonia gas exposure. The diffraction peak of AMP perovskite (101) at 25.35° was red-shifted after gas exposure and exhibited an amorphous structure, highlighted sudden changes in structural properties of the perovskite material. The roughness parameters of AMP increased while the same parameters for MIP decreased, highlighting AMP's greater potential as ammonia gas sensor that same trend as SEM images that samples were found to be more random and rougher compared to homogeneous morphology before gas exposure. It can be said that, MIP roughness decreased due to its self-crystallization because the substrate is thermodynamically unstable and easily converted to its original raw material of PbI_2. It is well confirmed from the literature that surface morphology and roughness of gas sensor materials represent their gas sensing potential. Although the stability of MIP is superior compared to AMP but AMP exhibits greater potential as gas sensor.

Author statement

Hasyiya Karimah Adli designed the experiments and checked the results, Norfatihah Mohd Adenam and Muhamad Yuzaini Azrai Mat Yunin performed the experiments. Norfatihah Mohd Adenam analyzed the data and wrote the paper. Wan M. Khairul checked the paper draft. Abdul Hafidz Yusoff processed the paper submission. All authors have read and agreed to the published version of the manuscript.

Declaration of Competing Interest

The authors declare that they have no known competing financial interests or personal relationships that could have appeared to influence the work reported in this paper.

Acknowledgments

References

[1] L. Mao, R.M. Kennard, B. Traore, W. Ke, C. Katan, J. Even, M.G. Kanatzidis, Seven-layered 2D hybrid lead iodide perovskites, Chem. 5 (10) (2019) 2593–2604.

[2] Y.F. Xu, M.Z. Yang, B.X. Chen, X.D. Wang, H.Y. Chen, D.B. Kuang, C.Y. Su, A CsPbBr$_3$ perovskite quantum dot/graphene oxide composite for photocatalytic CO$_2$ reduction, J. Am. Chem. Soc. 139 (16) (2017) 5660–5663.

[3] Y. Cheng, Q.D. Yang, J. Xiao, Q. Xue, H.W. Li, Z. Guan, S.W. Tsang, Decomposition of organometal halide perovskite films on zinc oxide nanoparticles, ACS Appl. Mater. Interfaces 7 (36) (2015) 19986–19993.

[4] R. Segovia, G. Qu, M. Peng, X. Sun, H. Shi, B. Gao, Evolution of photoluminescence, Raman, and structure of CH$_3$NH$_3$PbI$_3$ perovskite microwires under humidity exposure, Nanoscale Res. Lett. 13 (1) (2018) 1–8.

[5] B.A. Rosales, M.P. Hanrahan, B.W. Boote, A.J. Rossini, E.A. Smith, J. Vela, Lead halide perovskites: challenges and opportunities in advanced synthesis and spectroscopy, ACS Energy Lett. 2 (4) (2017) 906–914.

[6] P. Pistor, A. Ruiz, A. Cabot, V. Izquierdo-Roca, Advanced Raman spectroscopy of methylammonium lead iodide: development of a non-destructive characterisation methodology, Sci. Rep. 6 (1) (2016) 1–8.

[7] G. Liu, H. Zheng, J. Ye, S. Xu, L. Zhang, H. Xu, X. Pan, Mixed-phase low-dimensional perovskite-assisted interfacial lead directional management for stable perovskite solar cells with efficiency over 24%, ACS Energy Lett. 6 (12) (2021) 4395–4404.

[8] K. Lin, J. Xing, L.N. Quan, F.P.G. De Arquer, X. Gong, J. Lu, Z. Wei, Perovskite light-emitting diodes with external quantum efficiency exceeding 20 per cent, Nature 562 (7726) (2018) 245–248.

[9] H.K. Adli, T. Harada, S. Nakanishi, S. Ikeda, Effects of TiCl$_4$ treatment on the structural and electrochemical properties of a porous TiO$_2$ layer in CH$_3$NH$_3$PbI$_3$ perovskite solar cells, Phys. Chem. Chem. Phys. 19 (39) (2017) 26898–26905.

[10] H.K. Adli, T. Harada, S. Ito, S. Nakanishi, S. Ikeda, Effects of TiO$_2$ properties on performance of CH$_3$NH$_3$PbI$_3$ perovskite photovoltaic cells, MRS Adv. 1 (47) (2016) 3185–3190.

[11] S. Gharibzadeh, B. Abdollahi Nejand, M. Jakoby, T. Abzieher, D. Hauschild, S. Moghadamzadeh, U.W. Paetzold, Record open-circuit voltage wide-bandgap perovskite solar cells utilizing 2D/3D perovskite heterostructure, Adv. Energy Mater. 9 (21) (2019), 1803699.

[12] M.Y.A. Mat Yunin, N. Mohd Adenam, W.M. Khairul, A.H. Yusoff, H.K. Adli, Effect of stability of two-dimensional (2D) aminoethyl methacrylate perovskite using lead-based materials for ammonia gas sensor application, Polymers 14 (9) (2022) 1853.

[13] J.W. Lee, N.G. Park, Chemical approaches for stabilizing perovskite solar cells, Adv. Energy Mater. 10 (1) (2020), 1903249.

[14] S. Sasmal, S.K. Sharma, S. Chatterjee, A.J. Pal, S.P. Turaga, A.A. Bettiol, S. Valiyaveettil, Gas-induced confinement–deconfinement interplay in organic–inorganic hybrid perovskite thin film results in systematic band modulation, ACS Appl. Mater. Interfaces 11 (46) (2019) 43708–43718.

[15] Z. Chen, M. Liu, Z. Li, T. Shi, Y. Yang, H.L. Yip, Y. Cao, Stable Sn/Pb-based perovskite solar cells with a coherent 2D/3D interface, Iscience 9 (2018) 337–346.

[16] X. Xu, Y. Pan, Y. Zhong, R. Ran, Z. Shao, Ruddlesden–popper perovskites in electrocatalysis, Mater. Horiz. 7 (10) (2020) 2519–2565.

[17] M. Kim, G.H. Kim, T.K. Lee, I.W. Choi, H.W. Choi, Y. Jo, D.S. Kim, Methylammonium chloride induces intermediate phase stabilization for efficient perovskite solar cells, Joule 3 (9) (2019) 2179–2192.

[18] W.C. Chen, Y.H. Fang, L.G. Chen, F.C. Liang, Z.L. Yan, H. Ebe, C.C. Kuo, High luminescence and external quantum efficiency in perovskite quantum-dots light-emitting diodes featuring bilateral affinity to silver and short alkyl ligands, Chem. Eng. J. 414 (2021) 128866.

[19] H. Zheng, W. Wu, H. Xu, F. Zheng, G. Liu, X. Pan, Q. Chen, Self-additive low-dimensional ruddlesden–popper perovskite by the incorporation of glycine hydrochloride for high-performance and stable solar cells, Adv. Funct. Mater. 30 (15) (2020), 2000034.

[20] Y. Cao, G. Qi, C. Liu, L. Wang, Z. Ma, K. Wang, B. Zou, Pressure-tailored band gap engineering and structure evolution of cubic cesium lead iodide perovskite nanocrystals, J. Phys. Chem. C 122 (17) (2018) 9332–9338.

[21] S. Tan, I. Yavuz, M.H. Weber, T. Huang, C.H. Chen, R. Wang, Y. Yang, Shallow iodine defects accelerate the degradation of α-phase formamidinium perovskite, Joule 4 (11) (2020) 2426–2442.

[22] D. Ghosh, M.Y. Ali, D.K. Chaudhary, S. Bhattacharyya, Dependence of halide composition on the stability of highly efficient all-inorganic cesium lead halide perovskite quantum dot solar cells, Sol. Energy Mater. Sol. Cells 185 (2018) 28–35.

[23] M.I. Saidaminov, J. Kim, A. Jain, R. Quintero-Bermudez, H. Tan, G. Long and, E. H. Sargent, Suppression of atomic vacancies via incorporation of isovalent small ions to increase the stability of halide perovskite solar cells in ambient air, Nat. Energy 3 (8) (2018) 648–654.

[24] W. Jiao, J. He, L. Zhang, Synthesis and high ammonia gas sensitivity of (CH3NH3) PbBr$_3$-xIx perovskite thin film at room temperature, Sens. Actuators B 309 (2020), 127786.

[25] X. Bao, Y. Wang, Q. Zhu, N. Wang, D. Zhu, J. Wang, R. Yang, Efficient planar perovskite solar cells with large fill factor and excellent stability, J. Power Sources 297 (2015) 53–58.

[26] G. Li, Y. Zhang, J. Lin, X. Xu, S. Liu, J. Fang, J. Chu, Anomalous NH$_3$-induced resistance enhancement in halide perovskite MAPbI$_3$ film and gas sensing performance, J. Phys. Chem. Lett. 12 (46) (2021) 11339–11345.

[27] B. Zhao, Y. Lian, L. Cui, G. Divitini, G. Kusch, E. Ruggeri, R.H. Friend, Efficient light-emitting diodes from mixed-dimensional perovskites on a fluoride interface, Nat. Electron. 3 (11) (2020) 704–710.

[28] A.A. Parfenov, O.R. Yamilova, L.G. Gutsev, D.K. Sagdullina, A.V. Novikov, B. R. Ramachandran, P.A. Troshin, Highly sensitive and selective ammonia gas sensor based on FAPbCl$_3$ lead halide perovskites, J. Mater. Chem. C 9 (7) (2021) 2561–2568.

[29] Y. Xin, W. Shen, Z. Deng, J. Zhang, Highly emissive and color-tunable perovskite cross-linkers for luminescent polymer networks, ACS Appl. Mater. Interfaces 10 (34) (2018) 28971–28978.

[30] K. Xiao, R. Lin, Q. Han, Y. Hou, Z. Qin, H.T. Nguyen, H. Tan, All-perovskite tandem solar cells with 24.2% certified efficiency and area over 1 cm2 using surface-anchoring zwitterionic antioxidant, Nat. Energy 5 (11) (2020) 870–880.

[31] J. Yin, Y. Yuan, J. Ni, J. Guan, X. Zhou, Y. Liu, J. Zhang, CH$_3$NH$_3$PbBr$_3$–x I x quantum dots enhance bulk crystallization and interface charge transfer for

efficient and stable perovskite solar cells, ACS Appl. Mater. Interfaces 12 (43) (2020) 48861–48873.

[32] D. Liu, C. Yang, M. Bates, R.R. Lunt, Room temperature processing of inorganic perovskite films to enable flexible solar cells, Iscience 6 (2018) 272–279.

[33] Q. Zhao, A. Hazarika, X. Chen, S.P. Harvey, B.W. Larson, G.R. Teeter, J.M. Luther, High efficiency perovskite quantum dot solar cells with charge separating heterostructure, Nat. Commun. 10 (1) (2019) 1–8.

[34] K. Wang, Z. Jin, L. Liang, H. Bian, D. Bai, H. Wang, S. Liu, All-inorganic cesium lead iodide perovskite solar cells with stabilized efficiency beyond 15%, Nat. Commun. 9 (1) (2018) 1–8.

[35] A. Torres, F.J. Luque, J. Tortajada, M.E. Arroyo-de Dompablo, DFT investigation of Ca mobility in reduced-perovskite and oxidized-marokite oxides, Energy Storage Mater. 21 (2019) 354–360.

[36] J. Wu, Y. Chang, W. Lv, G. Jiang, Y. Sun, Y. Liu, W. Cao, Topochemical transformation of single crystalline $SrTiO_3$ microplatelets from $Bi_4Ti_3O_{12}$ precursors and their orientation-dependent surface piezoelectricity, CrystEngComm 20 (22) (2018) 3084–3095.

[37] K. Hills-Kimball, H. Yang, T. Cai, J. Wang, O. Chen, Recent advances in ligand design and engineering in lead halide perovskite nanocrystals, Adv. Sci. 8 (12) (2021) 2100214.

[38] R. Guo, D. Han, W. Chen, L. Dai, K. Ji, Q. Xiong, P. Müller-Buschbaum, Degradation mechanisms of perovskite solar cells under vacuum and one atmosphere of nitrogen, Nat. Energy 6 (10) (2021) 977–986.

[39] J. Ran, O. Dyck, X. Wang, B. Yang, D.B. Geohegan, K. Xiao, Electron-beam-related studies of halide perovskites: challenges and opportunities, Adv. Energy Mater. 10 (26) (2020) 1903191.

[40] B. Qiao, P. Song, J. Cao, S. Zhao, Z. Shen, D. Gao, X. Xu, Water-resistant, monodispersed and stably luminescent $CsPbBr_3$/$CsPb_2Br_5$ core–shell-like structure lead halide perovskite nanocrystals, Nanotechnology 28 (44) (2017) 445602.

[41] S. Zhang, G. Han, Intrinsic and environmental stability issues of perovskite photovoltaics, Prog. Energy 2 (2) (2020), 022002.

[42] D. Marongiu, M. Saba, F. Quochi, A. Mura, G. Bongiovanni, The role of excitons in 3D and 2D lead halide perovskites, J. Mater. Chem. C 7 (39) (2019) 12006–12018.

[43] J.L. Minns, P. Zajdel, D. Chernyshov, W. Van Beek, M.A. Green, Structure and interstitial iodide migration in hybrid perovskite methylammonium lead iodide, Nat. Commun. 8 (1) (2017) 1–5.

[44] S. Nair, J.V. Gohel, Introduction of P3HT-based gradient heterojunction layer to improve optoelectronic performance of low-cost carbon-based perovskite solar cell, Opt. Mater. 119 (119) (2021), 111366.

[45] Y. Wang, M.I. Dar, L.K. Ono, T. Zhang, M. Kan, Y. Li, Y. Zhao, Thermodynamically stabilized β-CsPbI3–based perovskite solar cells with efficiencies>18%, Science 365 (6453) (2019) 591–595.

[46] C.C. Boyd, R. Cheacharoen, T. Leijtens, M.D. McGehee, Understanding degradation mechanisms and improving stability of perovskite photovoltaics, Chem. Rev. 119 (5) (2018) 3418–3451.

[47] D. Zhang, Y. Fu, H. Zhan, C. Zhao, X. Gao, C. Qin, L. Wang, Suppressing thermal quenching via defect passivation for efficient quasi-2D perovskite light-emitting diodes, Light, Sci. Appl. 11 (1) (2022) 1–10.

[48] B. Putz, O. Milković, G. Mohanty, R. Ipach, L. Pethö, J. Milkovičová, J. Michler, Structural characterisation of Cu-Zr thin film combinatorial libraries with synchrotron radiation at the limit of crystallinity, Mater. Des. 218 (2022), 110675.

[49] A. Liu, H. Zhu, S. Bai, Y. Reo, T. Zou, M.G. Kim, Y.Y. Noh, High-performance inorganic metal halide perovskite transistors, Nat. Electron. 5 (2) (2022) 78–83.

[50] Q. Hu, Z. Deng, M. Hu, A. Zhao, Y. Zhang, Z. Tan, J. Tang, X-ray scintillation in lead-free double perovskite crystals, Sci. China Chem. 61 (12) (2018) 1581–1586.

[51] J. Wang, J. Zhang, Y. Zhou, H. Liu, Q. Xue, X. Li, A.K. Jen, Highly efficient all-inorganic perovskite solar cells with suppressed non-radiative recombination by a Lewis base, Nat. Commun. 11 (1) (2020) 1–9.

[52] J. Schlipf, L. Bießmann, L. Oesinghaus, E. Berger, E. Metwalli, J.A. Lercher, P. Müller-Buschbaum, In situ monitoring the uptake of moisture into hybrid perovskite thin films, J. Phys. Chem. Lett. 9 (8) (2018) 2015–2021.

[53] H. Zheng, S. Dai, K. Zhou, G. Liu, B. Zhang, A. Alsaedi, X. Pan, New-type highly stable 2D/3D perovskite materials: the effect of introducing ammonium cation on performance of perovskite solar cells, Sci. China Mater. 62 (4) (2019) 508–518.

[54] E.M. Benali, A. Benali, M. Bejar, E. Dhahri, V.A. Khomchenko, L. Peng, B.F. O. Costa, Structural, morphological and excellent gas sensing properties of La1−2xBaxBixFeO3 (0.00≤ x≤ 0.20) nanoparticles, J. Alloys Compd. 883 (2021), 160856.

[55] S. Sulaiman, S. Izman, M.B. Uday, M.F. Omar, Review on grain size effects on thermal conductivity in ZnO thermoelectric materials, RSC Adv. 12 (9) (2022) 5428–5438.

[56] B. Kim, S.I. Seok, Molecular aspects of organic cations affecting the humidity stability of perovskites, Energy Environ. Sci. 13 (3) (2020) 805–820.

[57] J.M. Howard, R. Lahoti, M.S. Leite, Imaging metal halide perovskites material and properties at the nanoscale, Adv. Energy Mater. 10 (26) (2020) 1903161.

[58] H. Si, S. Zhang, S. Ma, Z. Xiong, A. Kausar, Q. Liao, Y. Zhang, Emerging conductive atomic force microscopy for metal halide perovskite materials and solar cells, Adv. Energy Mater. 10 (10) (2020), 1903922.

[59] Y. Hui, Y.Y. Tan, L. Chen, Z.A. Nan, J.Z. Zhou, J.W. Yan, B.W. Mao, Stability of perovskite thin films under working condition: bias-dependent degradation and grain boundary effects, Adv. Funct. Mater. 31 (36) (2021), 2103894.

[60] A. Stern, S. Aharon, T. Binyamin, A. Karmi, D. Rotem, L. Etgar, D. Porath, Electrical characterization of individual cesium lead halide perovskite nanowires using conductive AFM, Adv. Mater. 32 (12) (2020), 1907812.

[61] A.E.A. Saif, Z.V. Ooi, Y.C. Teh, Substrate effect on structural and humidity sensing of sol-gel derived Er-BaTiO3 thin films, AIP Conf. Proc. 1835 (1) (2017), 020017.

[62] L.A. Muscarella, E.M. Hutter, S. Sanchez, C.D. Dieleman, T.J. Savenije, A. Hagfeldt, B. Ehrler, Crystal orientation and grain size: do they determine optoelectronic properties of MAPbI3 perovskite? J. Phys. Chem. Lett. 10 (20) (2019) 6010–6018.

[63] J.V. Patil, S.S. Mali, C.K. Hong, A thiourea additive-based quadruple cation lead halide perovskite with an ultra-large grain size for efficient perovskite solar cells, Nanoscale 11 (45) (2019) 21824–21833.

[64] C. Castillo, G. Cabello, B. Chornik, Y. Huentupil, G.E. Buono-Core, Characterization of photochemically grown Pd loaded WO3 thin films and its evaluation as ammonia gas sensor, J. Alloys Compd. 825 (2020), 154166.

[65] S. Ruan, J.L. Niu, N. Pai, H. Ebendorff-Heidepriem, Y.B. Cheng, Y. Ruan, C.R. McNeill, An optical fibre-based sensor for the detection of gaseous ammonia with methylammonium lead perovskite, J. Mater. Chem. C 6 (26) (2018) 6988–6995.

[66] Y. Zhou, M. Yang, W. Wu, A.L. Vasiliev, K. Zhu, N.P. Padture, Room-temperature crystallization of hybrid-perovskite thin films via solvent–solvent extraction for high-performance solar cells, J. Mater. Chem. A 3 (15) (2015) 8178–8184.

[67] Y. Zhou, N.P. Padture, Gas-induced formation/transformation of organic–inorganic halide perovskites, ACS Energy Lett. 2 (9) (2017) 2166–2176.

[68] N.L. Chang, A.W. Yi Ho-Baillie, P.A. Basore, T.L. Young, R. Evans, R.J. Egan, A manufacturing cost estimation method with uncertainty analysis and its application to perovskite on glass photovoltaic modules, Prog. Photovolt. Res. Appl. 25 (5) (2017) 390–405.

[69] A.D. Sheikh, V. Vhanalakar, A. Katware, K. Pawar, P.S. Patil, Two-step antisolvent precipitated MAPbI3-pellet-based robust room-temperature ammonia sensor, Adv. Mater. Technol. 4 (9) (2019), 1900251.

[70] D. Solis-Ibarra, I.C. Smith, H.I. Karunadasa, Post-synthetic halide conversion and selective halogen capture in hybrid perovskites, Chem. Sci. 6 (7) (2015) 4054–4059.

[71] G. Kakavelakis, E. Gagaoudakis, K. Petridis, V. Petromichelaki, V. Binas, G. Kiriakidis, E. Kymakis, Solution processed CH3NH3PbI3–x Cl x perovskite based self-powered ozone sensing element operated at room temperature, ACS Sens. 3 (1) (2018) 135–142.

[72] K.Y. Lee, J.C. Hsieh, C.A. Chen, W.L. Chen, H.F. Meng, C.J. Lu, H.W. Zan, Ultrasensitive detection of hydrogen sulfide gas based on perovskite vertical channel chemo-sensor, Sens. Actuators B 326 (2021), 128988.